

Journal of
Applied
Crystallography
ISSN 0021-8898
Editor: **Gernot Kostorz**

Characterization and modelling of germanium assembled crystals for the diffraction of thermal neutrons

Lucia Alianelli, Manuel Sánchez del Río and Roberto Felici

Copyright © International Union of Crystallography

Author(s) of this paper may load this reprint on their own web site provided that this cover page is retained. Republication of this article or its storage in electronic databases or the like is not permitted without prior permission in writing from the IUCr.

Characterization and modelling of germanium assembled crystals for the diffraction of thermal neutrons

Lucia Alianelli,^a Manuel Sánchez del Río^{b*} and Roberto Felici^c^aINFM and ILL, c/o ESRF, BP 220 38043 Grenoble CEDEX, France, ^bESRF, BP 220 38043 Grenoble CEDEX, France, and ^cINFM, c/o ESRF, BP 220 38043 Grenoble CEDEX, France. Correspondence e-mail: srio@esrf.fr

Two assembled germanium crystals, produced for use as neutron monochromators, are characterized by means of neutron and X-ray diffraction. The neutron and synchrotron experimental data (reflectivity profiles and topographs) are compared with calculations based on analytical models and Monte Carlo simulations. Our results show the limits of the standard theories and indicate that full Monte Carlo simulations can be a valid tool for interpreting real crystal reflectivities.

Received 3 November 2003
Accepted 23 June 2004© 2004 International Union of Crystallography
Printed in Great Britain – all rights reserved

1. Introduction

Neutron monochromators are often based on the use of Bragg diffraction by non-perfect crystals. Perfect crystals are not suitable because of their narrow angular acceptance, which limits the outgoing flux. On the other hand, imperfect crystals, or crystals in which atomic planes suffer some imperfections or distortion, have much wider diffraction profiles and therefore higher integrated reflectivities. The most commonly used imperfect crystals for neutron monochromators are mosaic crystals. They can be considered as a collection of micro-crystallites slightly misoriented with respect to a given direction. It is highly desirable to control the distribution and strength of this misorientation or mosaicity in order to match the experimental requirements of spectral and angular resolutions of the monochromated beam.

Germanium is a good candidate for use as a neutron monochromator because of its large coherent scattering length and small incoherent and absorption cross sections. Moreover, it is available in large perfect crystal ingots at a relatively low price. In order to use germanium as a neutron monochromator, some kind of distortion has to be introduced to increase the integrated reflectivity. Mosaic germanium monochromators are obtained by assembling thin wafers that have been deformed by alternate bending in a furnace. The total number of wafers is defined by the thickness needed to reflect the neutron beam efficiently. One of the advantages of these monochromators is the possibility of obtaining an anisotropic mosaic spread, which prevents neutron loss in the plane perpendicular to the scattering. The high-temperature plastic deformation of large perfect germanium crystals leads to a microstructural change with a resulting mosaic structure (Treviño & Mildner, 2004). The main difficulty is achieving mosaic crystals with a spatially homogeneous microstructure starting from a perfect single crystal. When these crystals are used as neutron monochromators, the presence of substructures

can have two effects: lowering the peak reflectivity and producing non-uniform wavelength and intensity distributions of the reflected neutron beam. It happens that, during the deformation process, the crystal faces can 'stick' in the hot press and prevent gliding of the crystal planes as a whole. This is the reason for the presence of substructures in the crystals.

The homogeneity of the plastically deformed crystals depends critically on their thickness, so that neutron monochromators of a suitable thickness require the stacking of several wafers (Axe *et al.*, 1994; Vogt *et al.*, 1994). The crystal assembling process consists of gluing in a hot press, using thin aluminium or tin foils, the crystal layers that were previously bent and flattened to achieve the desired mosaic spread. The same method can be employed to assemble crystals of cylindrical shape, in which case the wafers are simply plastically bent and then glued, without a previous introduction of mosaicity. The plastic deformation produced by the curvature is in general sufficient for creating the imperfections in the atomic planes necessary to reflect neutrons efficiently.

In this paper, we discuss the neutron and X-ray characterization of two crystals assembled at the monochromator laboratory of the ILL. Both samples were obtained by stacking ten wafers, each 1 mm thick. One is a flat crystal, in which the wafers have suffered a deformation process with a resulting anisotropic mosaicity, with an average full width at half-maximum (FWHM) larger in the direction of deformation. In the second sample, the non-deformed wafers are simply bent to a cylindrical shape and assembled. The integrated reflectivities of these two crystals are similar, though the applications can be different.

2. Methodology for the data analysis

Two main experimental methods are used in this paper: (a) neutron and X-ray (synchrotron radiation) reflectivity profiles and (b) X-ray diffraction topographs. Since the crystals

studied in this work are to be used as neutron monochromators, it is natural to characterize them by neutron diffraction. However, neutron beams are usually far from being an ideal probe to illustrate the microstructure of the crystal, as they usually have a large divergence and spectral bandwidth. It is therefore desirable to complement the information obtained by neutron diffraction with that obtained using synchrotron radiation. The high degree of collimation and monochromaticity presented by third-generation synchrotron radiation beams allows the measurement of diffraction profiles in almost ideal conditions. The recorded rocking curves can be compared directly with the theoretical profiles without further deconvolution. Moreover, using a micrometric beam, one can measure the diffracting properties on a very small scale giving an insight into the homogeneity of the crystal. This can be accomplished by means of X-ray topography. In the case of bent crystals, the measured rocking curves are the result of the convolution of the large divergent incident beam and the crystal reflectivity. Because the synchrotron beam has a negligible divergence with respect to the crystal angular diffraction range, it is straightforward to compare the measured rocking curves with the calculated diffraction profiles.

A summary of the experiments performed with the two samples under study is given in Table 1. The experimental rocking curves are fitted with diffraction profiles calculated using analytical formulae obtained for well known models. For flat mosaic crystals we use the mosaic model (Zachariasen, 1945; Sears, 1997), whereas for bent mosaic crystals we apply the layer coupling model (Hu & Fang, 1993). This model concerns mosaic crystals that have a distortion of the Bragg planes (bending or *d*-spacing gradient) along one direction.

The parameters adjusted in the fitting procedure were: the FWHM η of the mosaic distribution $W(\theta - \theta_B)$ (θ is the grazing angle and θ_B is the Bragg angle), the scattering factor Q and the attenuation coefficient μ . We recall that the FWHM of the reflectivity profile is strongly related to η , but the two quantities are not coincident. The need to fit μ follows from several considerations.

(i) The slope of the diffraction profile of a bent crystal, which is asymmetric, is characterized by the attenuation.

(ii) In the case of neutrons, the sources of attenuation of the incident and diffracted beams are the absorption by nuclei, the thermal diffuse scattering by phonons (TDS) and the parasitic Bragg scattering:

$$\mu = \mu_{\text{abs}} + \mu_{\text{TDS}} + \mu_{\text{par}} \quad (1)$$

The relative contribution of the three different terms in equation (1) depends on the neutron energy, the temperature, the Bragg planes and the crystal orientation. The absorption by nuclei has a linear dependence on wavelength and is not temperature dependent. μ_{TDS} is calculated as in the work of Freund (1983). μ_{par} includes all the intensity changes due to

Table 1

Experimental and geometrical details for the (311) germanium samples.

The attenuation coefficient was fixed for the flat sample ($\mu_{\text{fit}} = \mu_{\text{theor}}$).

Sample	Probe	Energy	Wave-length (Å)	Bragg angle (°)	μ_{theor} (cm ⁻¹)	μ_{fit} (cm ⁻¹)	Foot-print (mm)
Flat	Neutrons	30.4 meV	1.64	29	0.14	Fixed	0.485
Flat	X-rays	120 keV	0.103	1.7	1.8	Fixed	3.4
Flat	X-rays	90 keV	0.138	2.3	3.4	Fixed	2.5
Flat	X-rays	90 keV	0.138	7 ((933))	3.4	Fixed	2.5
Bent	Neutrons	20.4 meV	2	36	0.145	1	0.59
Bent	Neutrons	26.7 meV	1.75	31	0.14	0.75	0.515
Bent	X-rays	120 keV	0.103	1.7	1.8	2.2	3.4

scattering from simultaneously excited reflections or multiple Bragg reflections. We give an estimate of the effect of parasitic reflections in the case of the bent germanium neutron data and show that this effect can be seen as an increase of the effective attenuation coefficient.

(iii) For the X-ray analysis of the crystals, the effect of photoelectric absorption and Compton scattering have to be taken into account. We have treated Compton scattering as an additional source of attenuation. The use of high-energy X-rays minimizes the photoelectric absorption. On the other hand, Compton scattering increases with energy. For germanium, this contribution to the attenuation coefficient has the same value as the photoelectric effect at about 150 keV.

We have also measured X-ray topographs by using lamellar incident beams. The Bragg diffracted beam was recorded using a CCD camera, for different sample orientations. The profiles of the topographs depend on the local crystal properties and on the experimental parameters, such as beam size. As the shape and intensity of the topographs cannot be evaluated using direct analytic methods, we have developed a Monte Carlo code (Alianelli, 2002; Alianelli *et al.*, 2004) that simulates the beam propagation in imperfect crystals to reproduce numerically the topographs in a realistic way. The resulting simulations, which include experimental parameters such as the beam size, can therefore be compared directly with the experimental results.

3. Experimental

3.1. Neutron experiments

The neutron measurements were performed at the T13 instrument, a two-axes diffractometer used for crystal tests at the ILL (see Fig. 1). The beam was monochromated by a Ge (311) crystal, so that our measurements were taken in a Bragg symmetric geometry. Since the crystal arrangement was in the parallel configuration, the recorded diffraction profiles as a function of the crystal rocking angle were not influenced by the incident-beam divergence. The beam size and divergence were reduced by using absorbing diaphragms and Soller collimators after the monochromator.

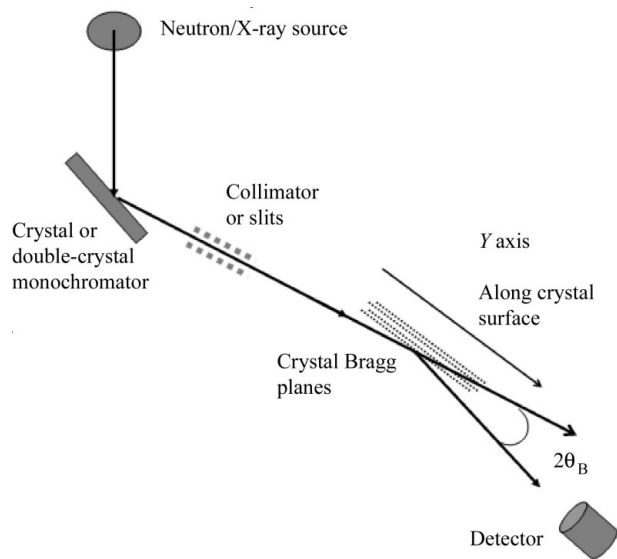


Figure 1
Schematic diagram of the geometry used for recording curves of reflected intensity. The Y axis is parallel to the crystal surface.

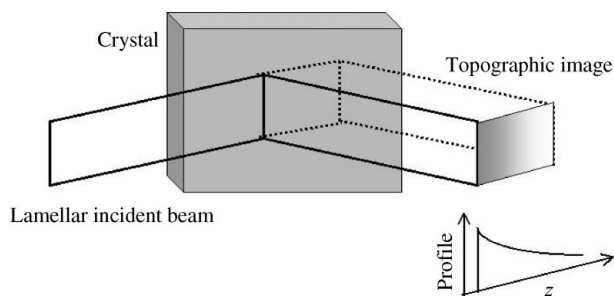


Figure 2
Topographic image recording. The dotted line represents the part of the beam which is diffracted after propagation in the crystal bulk. The schematic profile drawn at the bottom is obtained by integrating the image pixel values and represents the attenuation of the diffracted beam due to secondary extinction and absorption.

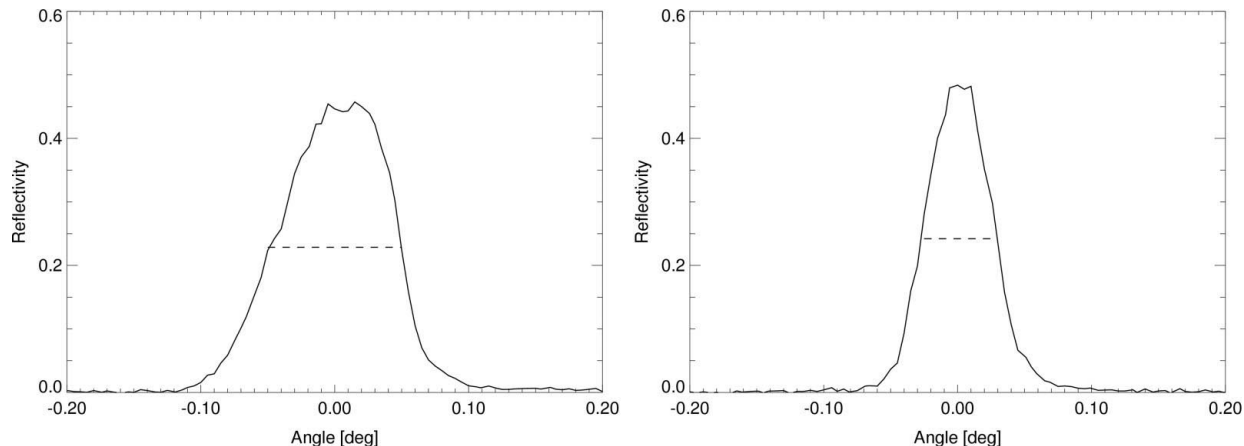


Figure 3
Experimental neutron reflectivity *versus* $(\theta - \theta_B)$ of the flat assembled crystal at $\lambda = 1.64 \text{ \AA}$. Left: the scattering plane corresponds to the direction in which the wafers were deformed. The reflectivity FWHM is 0.099° (intrinsic mosaicity $\eta_{\text{par}} = 0.07^\circ$). Right: scattering plane perpendicular to the direction of deformation. The reflectivity FWHM is 0.057° (intrinsic mosaicity $\eta_{\text{perp}} = 0.035^\circ$).

3.2. Synchrotron radiation experiments

The use of high-energy photons is required to guarantee that the beam penetrates into the crystal a reasonable distance (of the order of a few millimetres), as compared with the neutron beam which has larger attenuation lengths (of the order of 1 cm). X-rays with energies above 80 keV are available from an asymmetric wiggler at the beamline ID15A of the ESRF. The synchrotron white beam was monochromated by a perfect bent silicon crystal in Laue geometry. The energy resolution $\Delta E/E$ was of the order of $\sim 10^{-3}$.

The method of recording diffraction topographs is represented in Fig. 2. The incident X-ray beam width is defined by absorbing slits to a few tens of micrometres. The Bragg diffracted beam is recorded using a CCD camera placed perpendicular to the reflected beam. In principle, if an incident lamellar beam is used, the camera records the intensity diffracted by the Bragg planes along the beam path in the crystal bulk. However, as the beam has a finite width, the recorded image is the convolution of the finite beam size and the local crystal properties. If the crystal is homogeneous, the recorded image is a smooth function, showing a decrease of intensity in the direction of scattering because of attenuation and secondary extinction.

4. Results

4.1. Ge flat assembled crystal

4.1.1. Neutron experiment. Fig. 3 shows two neutron reflectivity profiles for the flat assembled germanium crystal. They were measured by rotating the azimuthal angle Φ of the crystal by 90° with respect to one another. The azimuthal asymmetry of the mosaic distribution produces reflectivity curves with azimuthal asymmetry, with FWHM values of 0.099 and 0.057° in the two perpendicular directions, respectively. The two diffraction profiles in Fig. 3 have approximately the same peak reflectivity. Two procedures can be used to reproduce these peak values. (a) We use an anisotropic mosaic distribution $W(\theta, \Phi)$ having a given peak value but different

Table 2

Fitting parameters of the X-ray data in Fig. 5: FWHM η and η_2 of $W(\theta - \theta_B)$, peak separation Δ and scattering factor Q .

Energy (keV)	90	90	120
hkl	311	933	311
θ_B ($^\circ$)	2.3	7	1.7
μ (cm^{-1})	3.4	3.4	1.8
η ($^\circ$)	0.05	0.035	0.1
η_2 ($^\circ$)	0.04	0.06	0.04
Δ ($^\circ$)	-0.062	0.055	0.07
Q_{theor} (cm^{-1})	0.0013	0.00007	0.0007
Q_{fit} (cm^{-1})	0.00105	0.000068	0.00065

widths for $\Phi = 0$ and $\Phi = 90^\circ$. The peak value is calculated by normalizing the integral of $W(\theta, \Phi)$ to unity. This method therefore gives a unique Q value for the two different scattering planes: $Q = 0.2Q_{\text{theor}}$. (b) We fit the two curves with two different independent distributions $W(\theta)$, having different peak values and widths. In order to reproduce the peak reflectivity properly with this method, we find $Q_{\text{par}} = 0.3Q_{\text{theor}} = 9.3 \times 10^{-4} \text{ cm}^{-1}$ and $Q_{\text{perp}} = 0.15Q_{\text{theor}} = 4.65 \times 10^{-4} \text{ cm}^{-1}$, respectively for the two perpendicular planes.

We observed that the peaks and widths of the experimental rocking curves depended on the region of the crystal illuminated by the beam. By shifting the crystal in the Y direction (*i.e.* along the projection of the incident beam onto the crystal surface), it is possible to obtain the variation of the diffraction intensity with this variable. The plots in Fig. 4 represent reflectivity as a function of angle and Y coordinate along the crystal length. The reflectivity looks smooth because of the poor spatial resolution of the beam (beam dimension of a few millimetres). By looking at the same data represented as contour curves, they show a displacement of the peak along Y , as if there were a residual bending of the Bragg planes in the bulk crystal.

4.1.2. Synchrotron experiment. Several X-ray rocking curves were measured at photon energies of 120 and 90 keV for the $\langle 311 \rangle$ reflection and its third harmonic (933) (Fig. 5).

The experimental data show the presence of grains, manifested by the presence of two or more overlapped peaks. Therefore, the fit was performed by using the mosaic model of Sears (1997) but with a mosaic distribution $W(\theta - \theta_B)$ given by the sum of two pseudo-Voigt functions with different FWHM values η_{fit} and $\eta_{\text{fit}2}$, shifted in angle by Δ with respect to each other. The fitting parameters are reported in Table 2. Fitting the data with a single-peak model (not shown) would give an average intrinsic mosaicity of $\eta \simeq 0.083^\circ$, of the same order as that obtained by analysing the neutron data ($\eta_{\text{par}} = 0.07^\circ$; see Fig. 3).

The presence of inhomogeneities is also shown by the diffraction profiles recorded for $\langle 311 \rangle$ at 90 and 120 keV along the crystal surface, as shown in Fig. 6. The peak reflectivity decreases by more than 50% over 10 mm along the surface. Furthermore, the surface plot at 90 keV shows some ripples. They are probably due to the non-ideally perfect flat shape caused by the deformation process. Contrary to the neutron data in Fig. 4, the position of the Bragg peak does not change with Y . By considering that the beam penetration is of the order of 100 μm (for the X-ray energies and angles reported here), we conclude that a possible residual bending is present in the crystal bulk but not at the surface.

4.2. Ge bent assembled crystal

4.2.1. Neutron experiment. The rocking curves of the $\langle 311 \rangle$ reflection with neutrons of $\lambda = 2$ and 1.75 \AA are reported in Fig. 7. The shape is a trapezoid (or triangular), which is typical of curved crystals. The angular spread of the incoming beam in the diffraction plane was $\Delta\theta \leq 0.02^\circ$ and may be neglected. The experimental peak reflectivity, for $\lambda = 2 \text{ \AA}$, is $\sim 60\%$. In the case of a perfect bent crystal, a peak reflectivity of 98% would be expected according to the lamellar model (Albertini *et al.*, 1976). The lower experimental peak reflectivity is explained by the presence of a mosaic distribution of the Bragg planes, which can be induced by the deformation and

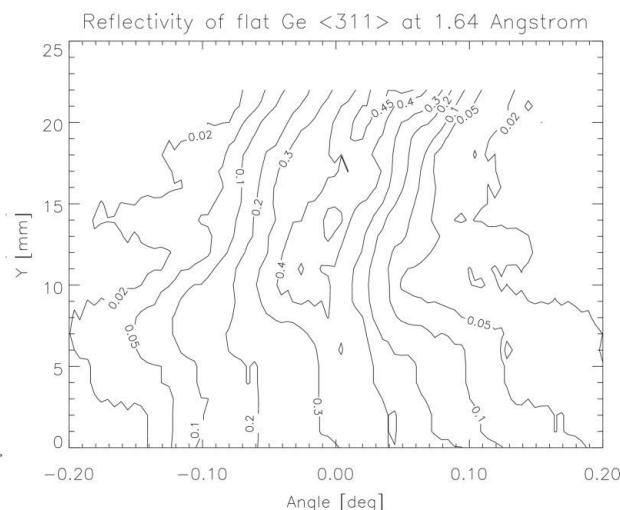
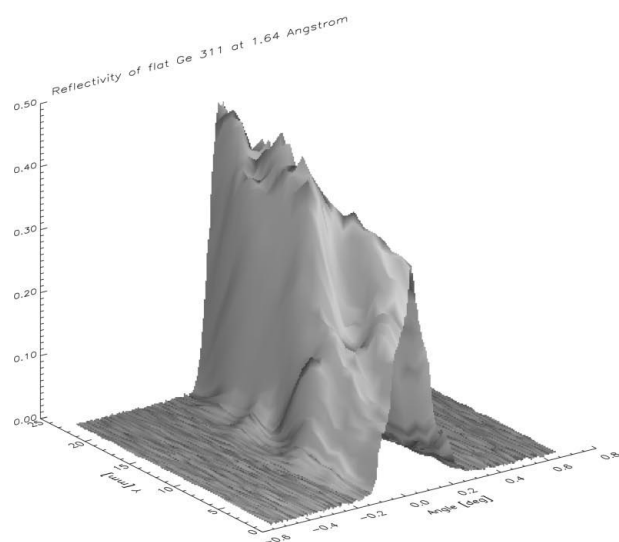


Figure 4

Neutron diffraction profiles *versus* angle and spatial coordinate Y , corresponding to the same experimental conditions as on the left in Fig. 3. Left: rocking curve recorded along the crystal surface. Right: contour of the plot on the left.

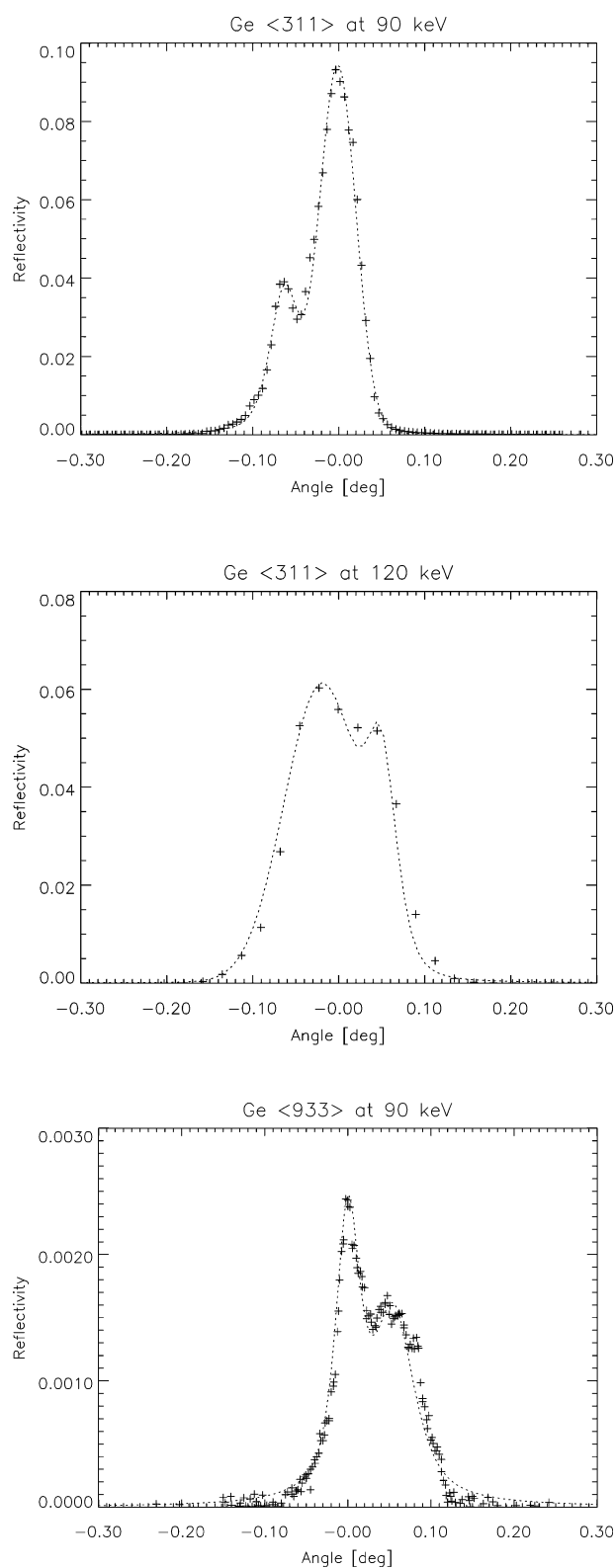


Figure 5
X-ray reflectivity versus $(\theta - \theta_B)$ of the assembled flat crystal (+ symbols). Top: (311) reflection at 90 keV. Middle: (311) reflection at 120 keV. Bottom: (933) reflection at 90 keV. The parameters used for calculating the theoretical reflectivity (dotted lines) using a mosaicity distribution $W(\theta - \theta_B)$ with two separate peaks are reported in Table 2.

gluing of the wafers. The fit parameters (the fits are the dashed lines) were mosaicity η , equivalent thickness d_{fit} and attenuation coefficient μ . These parameters are probably correlated to the scattering factor Q , so we do not include Q as a fitting parameter. According to Zachariassen (1945), a Q value smaller than the theoretical one accounts for primary extinction in small perfect crystallites and has the effect of lowering the peak reflectivity without changing the shape of the diffraction profile. In other words, correcting Q is essential when diffraction is governed by secondary extinction due to mosaicity, and when primary extinction is also present. In our case, the value of the fitted residual mosaicity is quite small as compared with usual mosaic crystals, and therefore neglecting this Q correction is a reasonably good approximation.

The fit shows a discrepancy between the real crystal thickness of $d = 10$ mm and the fitted reduced thickness $d_{\text{fit}} = 7$ mm. The explanation is not straightforward. One might simply say that d_{fit} is the thickness of the crystal volume seen by the beam, or the thickness corresponding to that part of the crystal which has not been damaged in the deformation and assembling process. Hence, for assembled crystals, the effective crystal volume used for diffraction is not simply determined by the geometrical thickness and the bending radius.

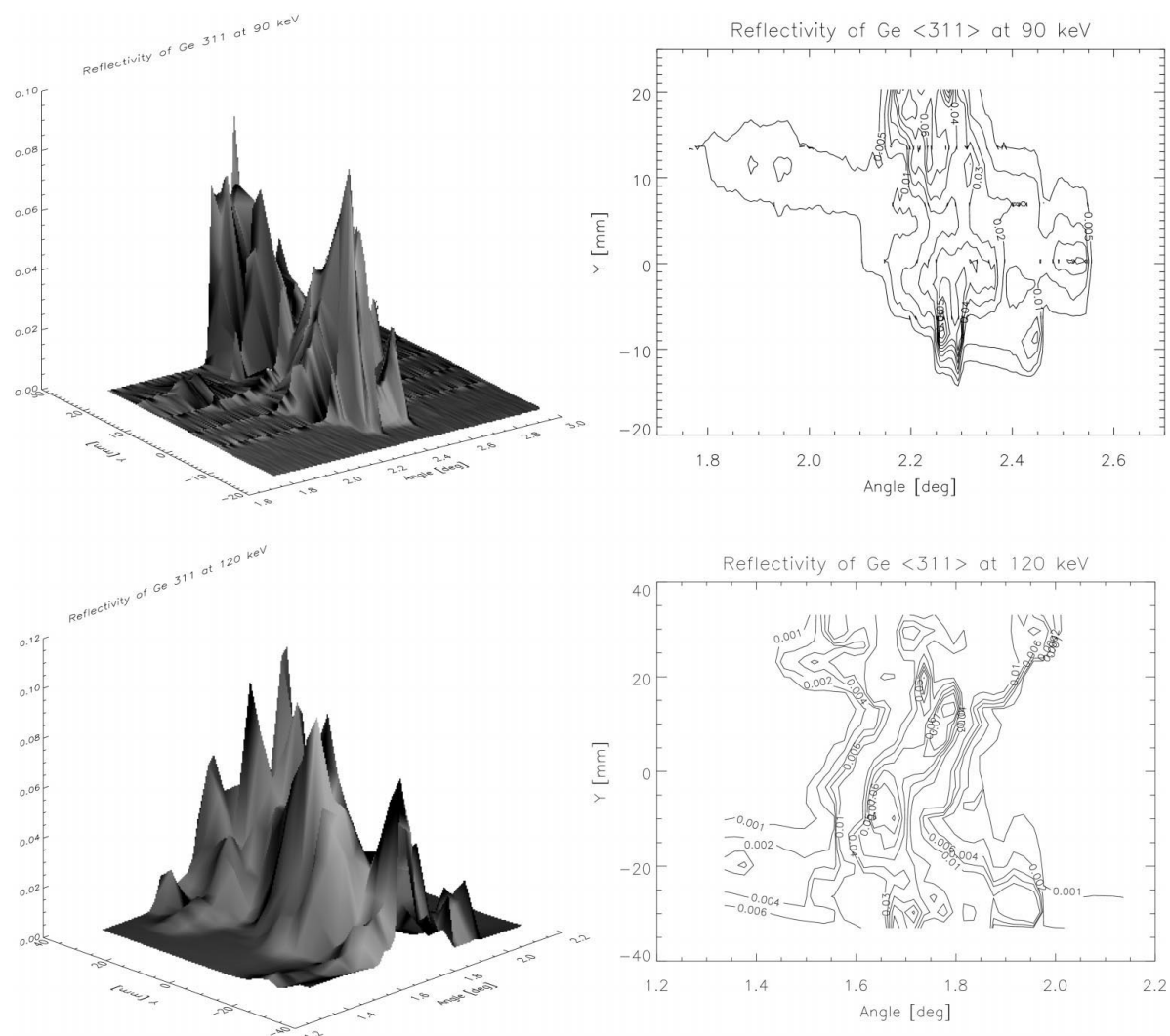
The fitted absorption coefficient is $\mu_{\text{fit}} = 1 \text{ cm}^{-1}$ at 2 \AA and $\mu_{\text{fit}} = 0.75 \text{ cm}^{-1}$ at 1.75 \AA . The calculations with $\mu_{\text{theor}} = \mu_{\text{abs}} + \mu_{\text{TDS}} = 0.14 \text{ cm}^{-1}$ (solid lines in Fig. 7) show a substantial increase of the integrated reflectivity. The high value of μ_{fit} can be partially explained by the presence of parasitic reflections or by the reduction of the coherent scattering volume due to the deformation and gluing of the wafers.

4.2.2. Synchrotron experiment. Rocking curves for the bent assembled crystal were recorded with a photon energy of 120 keV, in Bragg symmetric geometry. The profile in Fig. 8 shows a peak reflectivity of 18%, which is lower than that predicted by the lamellar theory for a bent perfect crystal (31%). The same effect was also seen for the neutron case. A mosaicity of $\eta_{\text{fit}} = 0.02^\circ$ was obtained from the fit. We also fitted μ because the experimental FWHM was narrower than the theoretical value and, as explained above, this is due to attenuation. The result was $\mu_{\text{fit}} = 2.2 \text{ cm}^{-1}$, whereas the theoretical value (neglecting parasitic scattering) is $\mu_{\text{theor}} = 1.8 \text{ cm}^{-1}$.

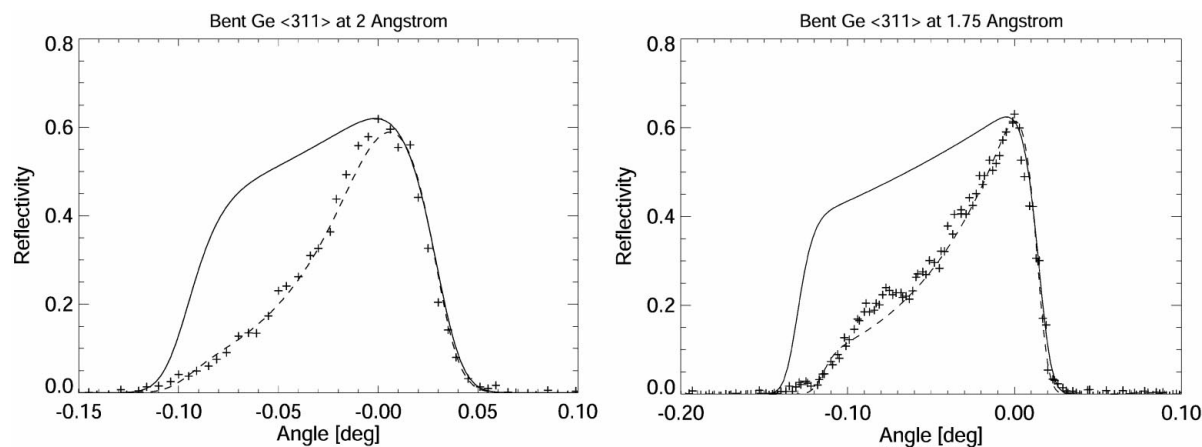
Some considerations of the homogeneity of the crystal can be obtained from the plot of the rocking curves at different positions Y along the crystal as shown in Fig. 9. The contour plot shows that there is an approximately linear variation of the angular position of the Bragg peak corresponding to the bending radius $R = 5.7$ m. The width of the rocking curve along Y is constant, but the peak reflectivity decreases with decreasing Y ; this is probably the effect of a smaller diffracting volume due to the limited crystal length (6 cm).

4.3. Discussion

The analysis of the neutron and synchrotron rocking curves for the flat assembled crystal has shown that experimental data can be interpreted using the standard model of mosaic crystals,


Figure 6

Left: X-ray rocking curves recorded as a function of Y along the crystal surface for the case shown in Fig. 5. The structures appearing on the tails, more visible in the upper surface plot, are due to real imperfections and not to noise or erroneous normalization. Right: contours of the plots on the left.


Figure 7

Experimental neutron reflectivity *versus* $(\theta - \theta_B)$ (+ symbols) of the bent crystal at 2 Å (left) and 1.75 Å (right). The dashed lines give the fit with the free parameters: mosaicity η , equivalent thickness d_{fit} and attenuation coefficient μ . The equivalent thickness is $d_{\text{fit}} = 7$ mm. The other parameters are: $\eta = 0.03^\circ$ and $\mu_{\text{fit}} = 1 \text{ cm}^{-1}$ (left); $\eta = 0.017^\circ$ and $\mu_{\text{fit}} = 0.75 \text{ cm}^{-1}$ (right). The actual crystal thickness was 10 mm and the calculated attenuation coefficients are $\mu_{\text{theor}} = 0.145 \text{ cm}^{-1}$ (for $\lambda = 2 \text{ \AA}$) and $\mu_{\text{theor}} = 0.14 \text{ cm}^{-1}$ (for $\lambda = 1.75 \text{ \AA}$). The solid lines correspond to a model with the nominal attenuation coefficient, an equivalent thickness of 9 mm, and mosaicity as specified above. In this case, in order to reproduce the peak reflectivity without fitting μ , it was necessary to use $Q = 0.5Q_{\text{theor}}$ (left) and $Q = 0.7Q_{\text{theor}}$ (right).

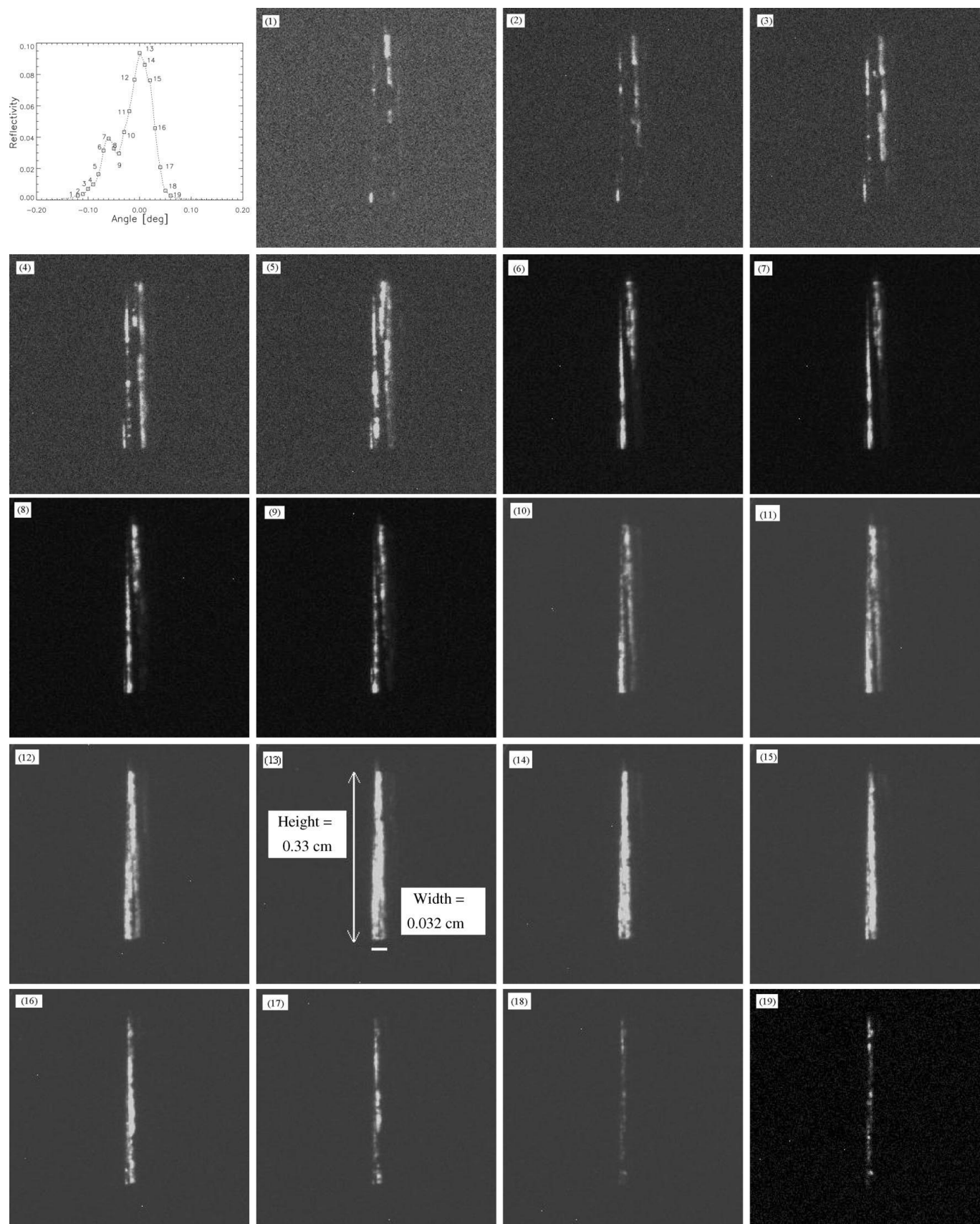


Figure 10

X-ray topographs of the assembled flat crystal at $E = 90$ keV for the (311) Bragg planes. The images were recorded at the angles indicated in the plot in the first row, with steps of 0.01° . The Bragg angle at this energy is 2.3° and the slit width was $100 \mu\text{m}$.

width of the rocking curve (apart from the bending radius which is not a fit parameter) is the crystal thickness, and this must be adjusted to an effective thickness in order to reproduce the experimental data.

(c) The slope of the reflectivity curve is determined by the attenuation factor. As shown in Fig. 7, we found an effective thickness of about 70% of the real one, and an attenuation factor of about five times the nominal value. This is probably due to parasitic reflections. In the case of X-rays (Fig. 8), the discrepancies between the fitted and the theoretical values are not so dramatic (+20%), because of the much higher attenuation of X-rays than of neutrons, making parasitic Bragg scattering less important. The intensity of parasitic reflections depends on the crystal mosaicity, orientation and on the incident-beam energy spread and divergence. Their approximate intensity can be calculated using the *MAMON* code (Sánchez del Río & Dejus, 1998), based on the method of Cole *et al.* (1962) for indexing the reflections. Their intensity is calculated with an approximated method, valid for powder crystals, described by Yvon *et al.* (1977). By considering an incident beam with $\Delta\lambda/\lambda = 5\%$ (of the same order as the resolution in the neutron measurements), the maximum neutron intensity subtracted by all the parasitic reflections, at $\lambda = 2 \text{ \AA}$, is $\sim 20\%$. This value would give an additional attenuation of the beam equal to $\mu_{\text{par}} = 0.07 \text{ cm}^{-1}$. This would give $\mu_{\text{theor}} = \mu_{\text{abs}} + \mu_{\text{TDS}} + \mu_{\text{par}} = 0.215 \text{ cm}^{-1}$, whereas we found $\mu_{\text{fit}} = 1 \text{ cm}^{-1}$. Hence the experimental value has to be explained by some other reason. Similar to the effective thickness, the high attenuation might originate from the reduction of the coherent scattering volume due to the deformation and gluing of the wafers.

5. X-ray topographs

X-ray topographs can be recorded for a direct visualization of the crystal blocks that contribute to the diffracted intensity. Figs. 10 ($E = 90 \text{ keV}$) and 11 ($E = 120 \text{ keV}$) report flat crystal images taken at different positions of the rocking curve (*i.e.* for several incident angles). These images clearly resolve layers, grains or blocks that contribute to the diffracted intensity. In the case of quite smooth topographs, as in positions (13) in Fig. 10 and (3) in Fig. 11, one can compare the horizontal line profile in the image (calculated by integration over the vertical direction) with results of simulations (Fig. 12). The numerical calculations were carried out using *MOSAIC*, a Monte Carlo code developed for the simulation of Bragg diffraction by imperfect crystals (Alianelli, 2002; Alianelli *et al.*, 2004). This program performs a detailed simulation of the beam propagation in the crystal and can therefore be used for detailed comparisons with experiments as presented here. For this, we need to define the geometry and energy of the incident beam, the crystallite thickness ($1 \mu\text{m}$ in our calculations) and misalignment distributions, and the physical parameters (material, attenuation coefficient, reflection and transmission probabilities, *etc.*). The code tracks many photon rays, calculating the full trajectory as it traverses or is reflected by the individual crystallite. Statistical analysis of the tracked rays gives information on several parameters that would be difficult to calculate from first principles, like multiple scattering, and simulates experimental data as in topography measurements.

An interesting question is whether the different illuminated zones in Figs. 10 and 11 correspond to different wafers or if

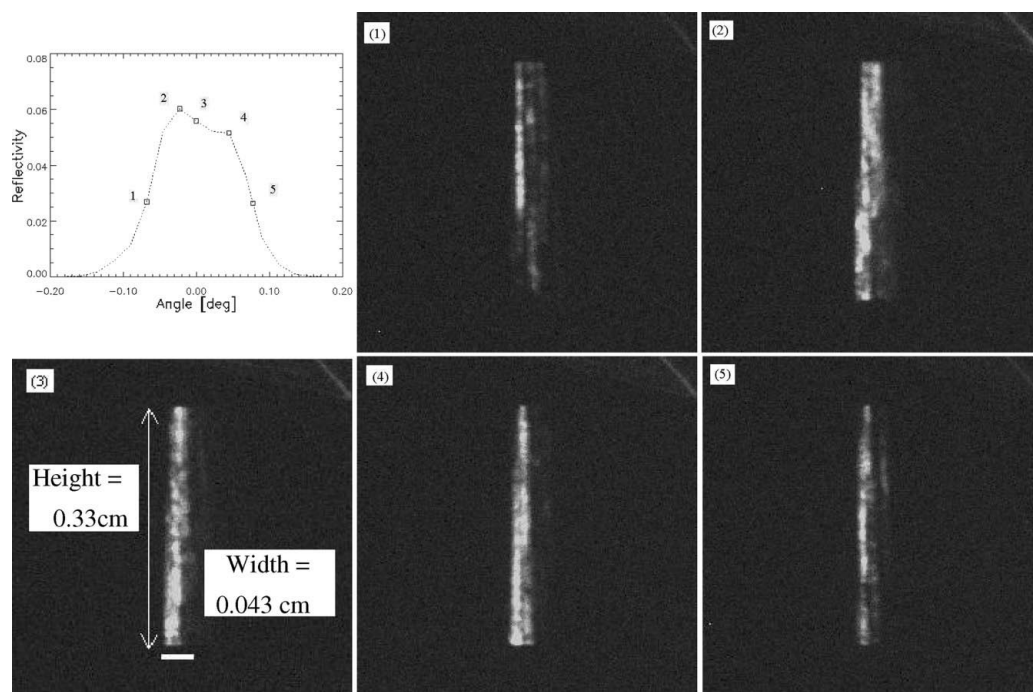


Figure 11

X-ray topographs of the assembled flat crystal at $E = 120 \text{ keV}$ for the $\{311\}$ Bragg planes. The angular positions at which the topographs were recorded are indicated as squares in the plot in the first row. The Bragg angle at this energy is 1.7° and the slit width was $100 \mu\text{m}$.

they are a proof of the ripples that appear also in the surface plot (see Fig. 6). We can assess this by comparing the simulation results to the image (5) in Fig. 10, corresponding to $\theta = \theta_B - 0.08^\circ$, and in positions where the structures are more visible. The *MOSAIC* program keeps track of the maximum depth reached by the simulated photon trajectories in the crystal. The simulation shows that, because of high attenuation, only those rays reaching a maximum penetration depth of approximately 0.4 mm have a non-negligible probability of being observed at the detector. Hence, according to the simulation result, the structures do not correspond to the wafer separa-

tion, but most probably to ripples in the first crystal wafer.

The topographs of the bent crystal (Fig. 13) show more uniform patterns than for the flat crystal; however, some structures are evident in the images labelled (1) and (2). If we compare the profile of the image labelled (6) with the Monte Carlo results using the value of μ obtained from the fit in Fig. 8, we find excellent agreement (Fig. 14). It is interesting to note that even though the crystal is bent, the profile is symmetric because of the convolution between the beam finite size and the bending of the crystal planes.

6. Conclusions

The experimental data and calculations provide a detailed characterization of two germanium samples that were produced for use as neutron monochromators. Neutron curves show good reflectivity, in agreement with the theory, but some parameters (scattering factor, attenuation coefficient, reduced thickness) need to be adjusted *ad hoc*. The X-ray analysis reveals some non-ideal features related to the inhomogeneous structure of the wafers forming the assembled crystals. The

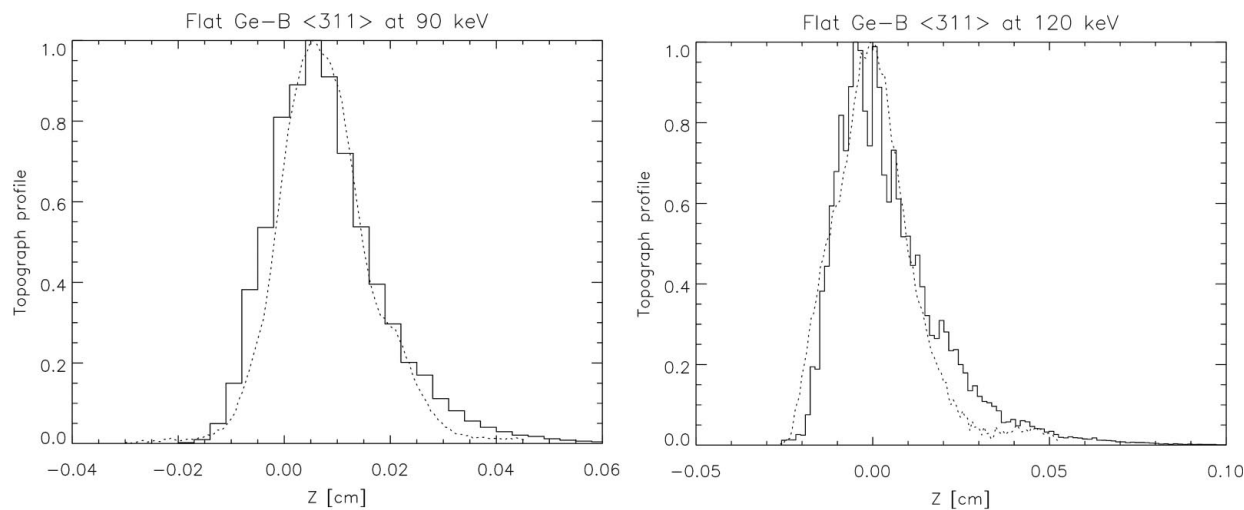


Figure 12

Flat assembled crystal: comparison between the experimental topograph profiles (dotted lines) and the histograms of the simulated topographs, weighted by using the theoretical attenuation coefficient. Left: profile of the experimental image number (13) in Fig. 10. Right: profile of the experimental image number (3) in Fig. 11. In the simulations, the perfect crystallite size is 1 μm . Their orientation is a Gaussian with FWHM equal to the intrinsic mosaicity η reported in Table 2.

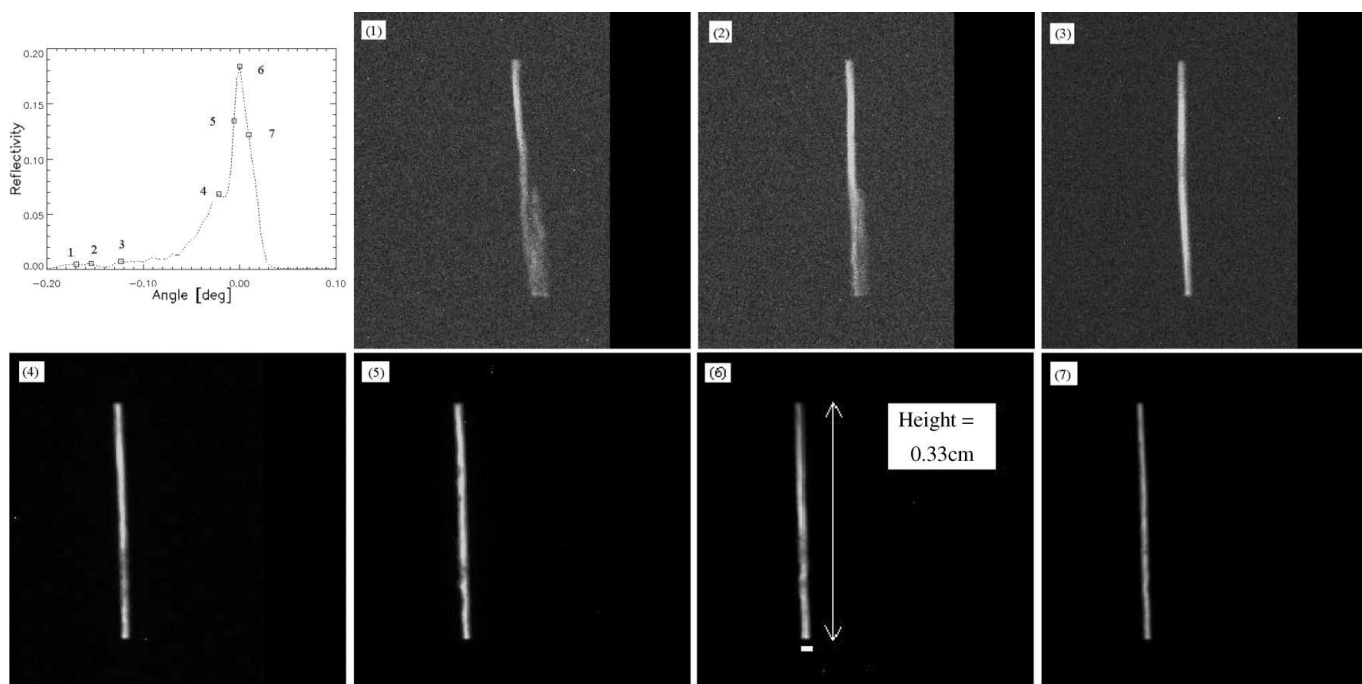


Figure 13

X-ray topographs of the assembled bent (311) Ge at $E = 120$ keV. The angular positions at which the topographs were recorded are indicated as squares in the plot in the first row. The Bragg angle at this energy is 1.7° and the slit width was 100 μm .

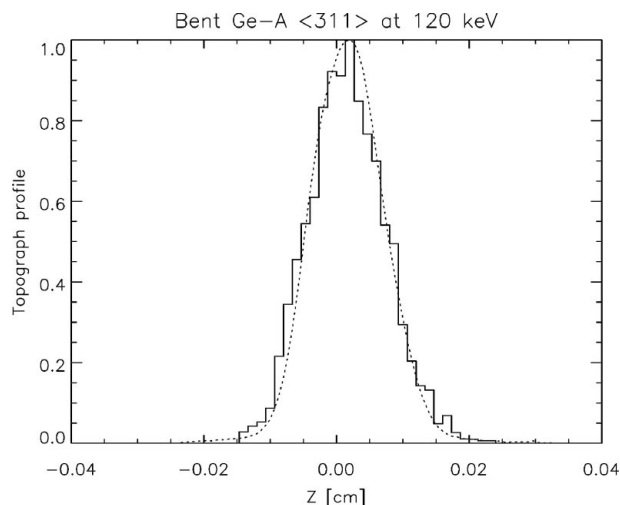


Figure 14

Topograph profiles for the $\langle 311 \rangle$ reflection from bent germanium at $E = 120 \text{ keV}$ at the exact Bragg angle. The dotted line corresponds to the experimental image number (6) in Fig. 13. The solid line is the histogram of the simulated X-ray topograph. The incident beam is $100 \mu\text{m}$ wide and 2 mm high and has a divergence of $20 \mu\text{rad}$. The crystal radius of curvature is $R = 5.7 \text{ m}$ and the attenuation coefficient $\mu = 2.2 \text{ cm}^{-1}$ (same value as the fit in Fig. 8). The perfect crystallites are $1 \mu\text{m}$ thick. Their orientation is a Gaussian with FWHM equal to $\eta = 0.02^\circ$. The image plane is 30 cm from the crystal.

reflectivity data have to be fitted with a mosaic distribution with more than one peak. This is also seen in the topographs that show the presence of ripples in the first wafer, especially for the flat (and more deformed) crystal. This paper presents a thorough characterization with different complementary techniques (X-ray and neutron beams, reflectivity and topography) of assembled germanium crystals. All experimental results are analysed with quantitative calculations, fits and Monte Carlo simulations. The results show the limits of the present theories and of the mosaic crystal fabrication technique.

We acknowledge the staff of the Monochromator Laboratory of the ILL. We are grateful to B. Hamelin and P. Courtois for providing the samples, for allowing access to the T13A and T13C instruments and the hard X-ray diffractometer and for the discussions about crystals and experiments. Many thanks are owed to E. Hetzler and R. Hehn for technical assistance. We wish to thank the ESRF, in particular the staff of the ID15A beamline, for professional help and assistance during the synchrotron experiments and their preparation. This work is partially financed by the SCANS RTD network, supported by the Access to Research Infrastructures activity, Improving Human Potential programme, of the European Commission under contract HPRI-CT-1999-50013.

References

- Albertini, G., Boeuf, A., Cesini, G., Mazkedian, S., Melone, S. & Rustichelli, F. (1976). *Acta Cryst.* **A32**, 863–868.
- Alianelli, L. (2002). *Characterization and Modelling of Imperfect Crystals for Thermal Neutron Diffraction*, PhD thesis, Université Joseph Fourier, Grenoble, France.
- Alianelli, L., Sánchez del Río, M., Felici, R., Andersen, K. H. & Farhi, E. (2004). *Physica B*. In the press.
- Axe, J. D., Cheung, S., Cox, D. E., Passell, L., Vogt, T. & Bar-Ziv, S. (1994). *J. Neutron Res.* **2**, 85–94.
- Cole, H., Chambers, F. W. & Dunn, H. M. (1962). *Acta Cryst.* **15**, 138–144.
- Freund, A. K. (1983). *Nucl. Instrum. Methods*, **213**, 495–501.
- Hu, H.-C. & Fang, Y. (1993). *J. Appl. Cryst.* **26**, 251–257.
- Sánchez del Río, M. & Dejus, R. J. (1998). *SPIE Proc.* **3448**, 340–345.
- Sears, V. F. (1997). *Acta Cryst.* **A53**, 35–45.
- Treviño, S. F. & Mildner, D. F. R. (2004). *J. Appl. Cryst.* **37**, 339–340.
- Vogt, T., Passell, L., Cheung, S. & Axe, J. D. (1994). *Nucl. Instrum. Methods A*, **338**, 71–77.
- Yvon, K., Jeitschko, W. & Parthé, E. (1977). *J. Appl. Cryst.* **10**, 73–74.
- Zachariasen, W. H. (1945). *Theory of X-ray Diffraction in Crystals*. New York: Dover.